Nanoscale

PAPER

View Article Online
View Journal | View Issue

Cite this: *Nanoscale*, 2025, **17**, 17733

Bimodal interfacial charge transfer in quantum dot heterostructures revealed by donor-/acceptor-specific broadband transient absorption spectroscopy†

Conner P. Dykstra, ‡[a] Thomas C. Rossi, [b] Michael J. Enright, [d] Josh Vura-Weis [a] and Renske M. van der Veen *[a,b,c]

Quantum dot sensitized metal–oxide heterostructures offer an attractive platform for harvesting carriers from solar energy. Interfacial charge transfer processes lie at the heart of solar energy conversion using heterostructured nanomaterials, yet they are poorly understood and difficult to study. Here we employ broadband optical transient absorption spectroscopy, spanning a wavelength range that covers both quantum-dot donor and metal–oxide acceptor band gaps, enabling a selective view of charge transfer across the interface of CdSe-sensitized ZnO nanorods. This allows us to reveal a bimodal charge injection mechanism: a fast (<1 ps) indirect charge injection pathway populates an optically dark intermediate state, and a direct charge injection pathway on the tens of ps time scale without an observable intermediate state. The bimodal charge injection kinetics are attributed to heterogeneity of ZnO acceptor states. Our results deepen the understanding of the role of donor and acceptor states in heterostructured nanomaterials and pave the way for the rational design and control of charge transfer across complex interfaces and their application in optoelectronic devices.

Received 14th February 2025,
Accepted 27th June 2025

DOI: 10.1039/d5nr00654f

rsc.li/nanoscale

1. Introduction

Understanding the parameters that govern interfacial charge transfer and separation is critical to realizing the next generation of photovoltaic devices.[1] Quantum dot sensitized metal–oxide heterostructures (QDH) are promising candidates for their tunable optical and electronic properties, fast charge transport attributes, and strong light absorption. Assembled by sensitizing a wide band-gap electron acceptor, like a metal oxide (MO), with a quantum dot (QD), a 0-dimensional semiconductor nanocrystal,[2] these materials leverage the tunability of QD energy levels and large absorption cross sections. Quantum confinement also promotes exotic carrier effects such as multi-exciton generation and hot electron transfer to bolster the efficiency of harvesting solar energy.[3–8] The efficiency of QDH devices is limited by non-radiative recombination pathways in the respective materials, which inhibits carrier separation and transport after injection at the QD–MO interface.[9,10] The large specific surface area of QDs make them sensitive to surface defects and undercoordinated atoms that form sub-band gap trap states for excitons and free carriers.[11–14] Nanostructured metal oxides, as either electron or hole acceptors, offer high surface area for sensitization, but at the cost of a high density of native defects.[15,16] Due to these complexities, a precise understanding of carrier separation dynamics across QDH interfaces is still lacking.

The QDH interface has an energetic landscape altered by undercoordinated surface atoms, adsorbed organic species, and the electronic coupling between the electron donor and acceptor materials.[17–19] While TiO_2 is the most studied MO electron acceptor, ZnO is a promising alternative due to its direct band gap, comparable electron mobility, low mineral cost, and easy solution-phase manufacturing into various nanostructures.[20,21] Despite these advantages, slower electron injection times are typically observed at ZnO interfaces compared to TiO_2, which have been attributed to a lower density of states (DOS) above the band gap,[22] defects at the

[a]*Department of Chemistry and Materials Research Laboratory, University of Illinois at Urbana-Champaign, 61801 Urbana, USA*
[b]*Department of Atomic-Scale Dynamics in Light-Energy Conversion, Helmholtz Zentrum Berlin für Materialien und Energie GmbH, 14109 Berlin, Germany. E-mail: renske.vanderveen@helmholtz-berlin.de*
[c]*Institute of Optics and Atomic Physics, Technical University of Berlin, 10623 Berlin, Germany*
[d]*Department of Chemistry and Biochemistry, San Francisco State University, 94132 San Francisco, USA*
†Electronic supplementary information (ESI) available. See DOI: https://doi.org/10.1039/d5nr00654f
‡Present address: Department of Chemistry and Biochemistry, The Ohio State University, Columbus, Ohio 43210, USA.

surface,[12] and the formation of an interfacial charge transfer state.[23–29]

The study of charge carrier transfer across the interface of QDHs is challenging for several reasons. First, the properties of nanomaterials are very sensitive to the sample's processing and synthetic history and are affected by the inherent heterogeneity of prepared materials.[30,31] Additionally, surface-sensitive techniques, such as time-resolved X-ray photoelectron spectroscopy (XPS), are difficult to apply to buried interfaces in heterostructured nanomaterials. Other commonly used techniques to study interfacial charge transfer processes are transient infrared (IR), time-resolved terahertz (THz), and optical transient absorption (OTA) spectroscopies.[28,32–35] Each of these techniques is powerful in certain ways but have critical corresponding limitations. Transient IR spectroscopy is sensitive to hole dynamics in the QDs but suffers from overlapping signals from free carriers in the metal oxide.[36–38] Time-resolved THz spectroscopy probes the conductivity of free carriers in the MO conduction band, but can have interference from mobile carriers in the QDs with limited ability to distinguish between the two types of carriers.[28,29,39] OTA in the visible region (~400 to 800 nm) is sensitive to the electron population of the QDs, but cannot distinguish between a depletion of the excited carrier population due to electron injection *vs.* trapping at surface defects.[32,40,41]

In this article, broadband ultraviolet (UV)/visible transient absorption spectroscopy is employed to track the evolution of the total excited carrier population from the initial excitation in CdSe QDs (donor) through charge transfer into ZnO nanorods (acceptor). The broad spectral probing range covers the ZnO direct band gap in the UV (~3.3 eV) as well as the spectrally distinct CdSe QD band gap in the visible (~2.1–2.6 eV).[42] This enables the selective probing of band gap transitions of both materials within a single technique, rendering it a powerful tool for correlating the arrival of carriers in the ZnO bulk DOS with the depletion of carriers in the CdSe QDs. Through careful analysis of both the amplitude and kinetics at both band gap transitions and looking at the effect of the density of acceptor states and QD sizes, we show that charge transfer proceeds through a short-lived intermediate state into heterogeneous acceptor states (HAS), and distinguish two timescales for charge injection: sub- or few-picosecond (ps) and tens of ps. A strategy of wide-scale sampling is employed to ensure robust and statistically relevant results from QDHs, and global fitting is used to support a proposed kinetic model that encompasses carrier dynamics in both ZnO and CdSe. To demonstrate the sensitivity of this technique to acceptor states and support the attribution of bimodal injection to HAS, two additional parameters were screened (the density of acceptor states and QD size) and found to be consistent with the proposed model. The observation of two charge transfer timescales, from both the donor and acceptor vantage points, demonstrates with clarity that both materials contribute to shaping the energetic landscape.

2. Methods

2.1. Materials synthesis

ZnO nanorods were grown by a well-established hydrothermal method.[43–46] The detailed synthesis procedures for the ZnO nanorods and CdSe QDs are included in the ESI S1.† The process of chemically linking the QDs to the MO support involves a phase transfer to polar solvent via ligand exchange of the native oleate (OA) surface with 3-mercaptopropionic acid (MPA) ligands. The latter are bifunctional ligands that coordinate with their sulfide moieties to the QDs and carboxylic acid to the ZnO surface. Conjugation was done by first heating the ZnO nanorods in a vacuum oven at 70 °C, then immediately immersing them in the QD solution. The mixture was kept at 50 °C under nitrogen, and in the dark, for approximately 12 hours. The ZnO nanorods were then washed with ethanol and stored under nitrogen in the dark. If desired, after nanorod growth these samples were annealed (A-ZnO) prior to QD sensitization. Annealing was done in a tube furnace by ramping to 150 °C at a rate of 10 °C min^{-1} and held for 10 minutes, then heated to 400 °C and annealed for 20 min under argon.

2.2. Broadband transient absorption spectroscopy

Transient absorption spectroscopy experiments were performed at the Materials Research Laboratory (MRL) at the University of Illinois Urbana-Champaign. In brief, a 1 mm thick CaF_2 window or a 1 mm sapphire window was pumped with 800 nm light pulses (~120 fs, 1 kHz) to produce probe pulses with a spectrum covering 350–750 nm (visible probe), or with 400 nm light pulses (~120 fs, 1 kHz) to produce probe pulses with a spectrum covering 250–400 nm (UV probe). The CdSe QDs were excited with ~120 fs pulses at 513 nm (2.42 eV). The latter is close to the band gap of 2.6 nm CdSe QDs (2.41 eV) such that carrier cooling and impact ionization effects are minimized. The laser fluence used in all measurements (~60–72 μJ cm^{-2}) minimized the number of biexcitonic states while achieving a reasonable signal magnitude. It resulted in an average exciton population $\langle N \rangle$ = 0.2 per QD (details in S2†). Signal magnitudes were typically 500 μOD in the visible and UV ranges. Reference measurements were conducted on the CdSe QDs in solution with their native organic coating, with an identical $\langle N \rangle$ of 0.2, at a fluence of ~20 μJ cm^{-2} (shown in S3†). The measurements of QDs with different sizes and kinetic traces are discussed in S4.†

2.3. Measurement strategy and analysis

QDH materials are inherently heterogeneous, which warrants a careful measurement strategy in order to achieve statistically significant results.[47] In order to average out variations as a function of probing location, pump–probe measurements were performed a minimum of five different spots across the whole sample surface for both spectral probing ranges (UV and visible), and without overlapping spots. At least three two-dimensional wavelength-time delay data sets were acquired

and averaged per sample spot. Kinetic traces were extracted at wavelengths that avoided pump scatter and optimized statistics, while avoiding overlapping transitions. For sensitized ZnO in the UV this was 365 nm, and in the visible was 500 nm. Since solution phase CdSe has sharper electronic transitions, kinetic traces were taken at 490 nm to allow more of the 1st excitonic transition to be integrated to yield kinetics representative of the 1st excitonic transition. Kinetic traces extracted from these averaged data sets were fitted to a sum of exponential functions, weighted by the error bars from the average. To prevent overfitting and determine the maximum number of components to be included in the fit, the Aikake and Bayesian information criteria were applied (see S5†).[48,49] The fitted time constants and amplitudes for different sample spots were averaged together and their errors were propagated, resulting in a set of fitted parameters (and their errors) for each probing region. The fitted amplitudes were normalized per probing region such that the sum of amplitudes adds to 100%. Samples were kept under a flowing nitrogen atmosphere for the duration of the experiment and no change in kinetics was found between the first and last measurement per sample spot (see S6 and S7†). Annealed ZnO samples had greater pump scatter on average, thus kinetic traces were taken at 495 nm to limit this impact.

3. Results and discussion

3.1. Materials characterization

The integrity of the QDs after phase transfer was confirmed by UV-Visible absorption spectroscopy, shown in Fig. 1(a). The CdSe QDs have a lowest energy excitonic transition, $1S_e$–$1S_{h_{3/2}}$, located at 515 nm (2.41 eV), corresponding to an average QD diameter of 2.6 ± 0.1 nm (S1†).[50] The energy and full width half maximum (FWHM) of this excitonic transition remain unchanged upon ligand exchange and phase transfer, indicating that the size distribution of the QDs is preserved. A slight solvatochromic shift is observed due to a change in the solvent dielectric constant (hexane for the OA ligands and methanol for the MPA ligands). Two higher excitonic transitions, $1S_e$–$2S_{h_{3/2}}$ and $1P_e$–$1P_{h_{3/2}}$, are visible around 470 nm and 415 nm, respectively.

Neat ZnO nanorods feature a sharp absorption onset near the ZnO band gap ~375 nm, along with an extended tail below the band gap. The latter is due to a combination of sub-band gap states (Urbach tail) arising from crystalline disorder and to Mie scattering from the densely packed nanorods.[51–53] ZnO nanorods have a band gap of 3.26 eV. After annealing their band gap amounts to 3.22 eV as obtained with a Tauc fit (S8†).

The UV-Visible spectrum after sensitization of the ZnO nanorods with the MPA-coated 2.6 ± 0.1 nm CdSe QDs is also shown in Fig. 1(a). The QD-sensitized ZnO features a small absorption transition at the CdSe first excitonic transition. Based on the absorption increase at 515 nm following CdSe sensitization, the ZnO surface area estimated from SEM, and assuming spherical close packing, the CdSe QD coverage is estimated to be 8% of a full monolayer on as-synthesized ZnO and 12% on annealed ZnO (see S8† for details). The baseline between sensitized and unsensitized ZnO was aligned at wavelengths far above 515 nm due to adsorption induced disorder at the surface and a slight increase of the Mie scattering cross-section upon sensitization.[42,54–56] Further materials characterization results are provided in S8.† QDs with both larger and smaller diameters were synthesized and used to sensitize unannealed ZnO, as shown in S8.† The sensitization

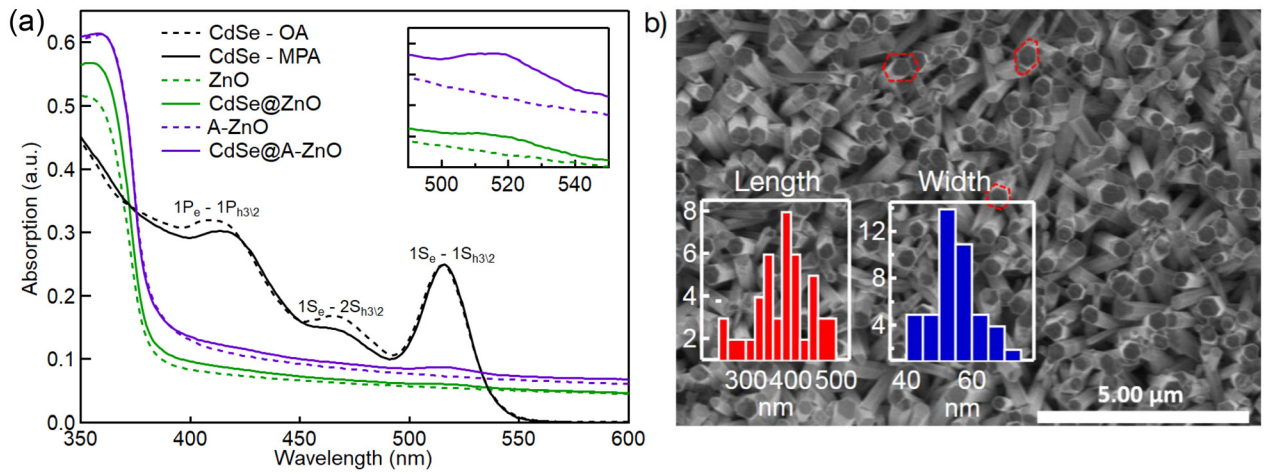

Fig. 1 (a) Static UV/visible absorption spectrum of 2.6 ± 0.1 nm CdSe QDs before and after exchanging the oleic acid (OA) ligands (hexane solvent, dashed black) with the 3-mercaptopropionic acid (MPA) ligands (methanol solvent, solid black). The absorption spectrum of the neat ZnO nanorods prior to sensitization is shown in dashed green (dashed purple for annealed ZnO) and the spectrum of CdSe-sensitized ZnO nanorods (CdSe@ZnO, or CdSe@A-ZnO when annealed) is shown in solid green (solid purple) after aligning the baseline. The inset shows a zoom into the spectral region of the first excitonic peak of the ZnO and QD–ZnO materials. (b) SEM image of the *c*-axis oriented ZnO nanorods, with a few (0001) faces highlighted in red. The size histograms are shown as an inset.

procedure for these systems was identical to the procedure listed above.

As shown in Fig. 1b, the ZnO nanorod synthesis produces a nanorod array with highly crystalline, hexagonal wurtzite nanorods that are ~380 ± 60 nm long and 60 ± 10 nm wide, ~50° tilt from the surface normal, and a density of 158 nanorods per μm^2. Additional SEM and TEM images can be found in S8.† Annealing ZnO results in a multitude of changes, such as improved crystallinity and reduced defect concentration as seen with XRD and PL respectively (S8†). The degree of crystallinity and concentration of defects is expected to lower the rate of trapping and potentially improve the quantum yield of charge transfer. The most impactful effect in the context of charge injection kinetics is the removal of surface adsorbates from the undercoordinated ZnO surface, as seen with FTIR (S8†). Surface adsorbates can cause a high magnitude of band bending in ZnO.[17,19,57–60] Contrary to nonpolar *a*- $(10\bar{1}0)$ and *m*-plane $(11\bar{2}0)$ ZnO facets, contaminants adsorbed on the Zn-terminated (0001) surface are stable up to 700 °C.[17] Since these nanorods are well oriented with the (0001) facet oriented approximately normal to the X-rays, there may be a preference for this facet of ZnO in the XPS measurements. Annealing at the relatively low temperature of 400 °C does not completely remove organic contaminants, which is confirmed from the elemental ratios obtained *via* XPS shown in Fig. 2. Before annealing, the atomic ratios are 39.5% carbon, 44% oxygen, and 16.5% zinc. After annealing, oxygen increases to 50.1%, zinc increases to 23.8%, and carbon decreases to 26.1%.

As seen in Fig. 2a the O 1s spectrum required 3 Gaussian contributions to be fit adequately, which are attributed to surface hydroxide, lattice bound oxygen, and oxygen vacancies (V_O).[61] Annealing shows reduced concentrations of surface hydroxide and V_O. A corresponding shift of the O 1s peak by 150 meV to lower binding energies is also seen. The Zn 3d spectrum required two Gaussian contributions to be fit, a single skewed-Gaussian was not adequate. As shown in Fig. 2b, the total envelope shifts toward lower binding energies, which is attributed to a reduction in the magnitude of downward band bending near the surface. The Zn 3d character shifts by ~120 meV to lower binding energies after annealing, along with a narrowing of the FWHM by 70 meV. The detailed fitted parameters can be found in Tables S2 and S3.† As previously interpreted in ref. 19 and 60, the reduced elemental carbon percentage, peak shifts, and peak narrowing are attributed to a reduction in downward band bending of the valence and conduction bands near the surface, resulting from a removal of surface adsorbates.[62]

3.2. Spectral analysis

Fig. 3a shows a typical 2D wavelength–time plot of the UV and visible transient absorption spectra of CdSe@ZnO upon excitation at 513 nm. The data is characterized by two prominent depleted absorption (bleach) features at ~360 nm and ~510 nm, which are located near the band edges of ZnO and CdSe, respectively. Both features are due to phase space filling (PSF, a contribution of Pauli blocking) of the band-gap edges by photogenerated carriers, which makes dual UV-Visible probe transient absorption spectroscopy sensitive to the carrier population dynamics in both the electron donor (CdSe QDs) and acceptor (ZnO nanorods) materials. The PSF signal in ZnO is due solely to injected electrons because the QDH has a type II (staggered) band alignment (Fig. 3b).[63] The excited-state absorption (ESA) feature below 350 nm is due to a Drude like response of free carriers in the conduction band, resulting in a change in the real part of the ZnO refractive index.[64,65] In CdSe, the transient signal at the band gap is predominantly sensitive to the photogenerated electron population in the con-

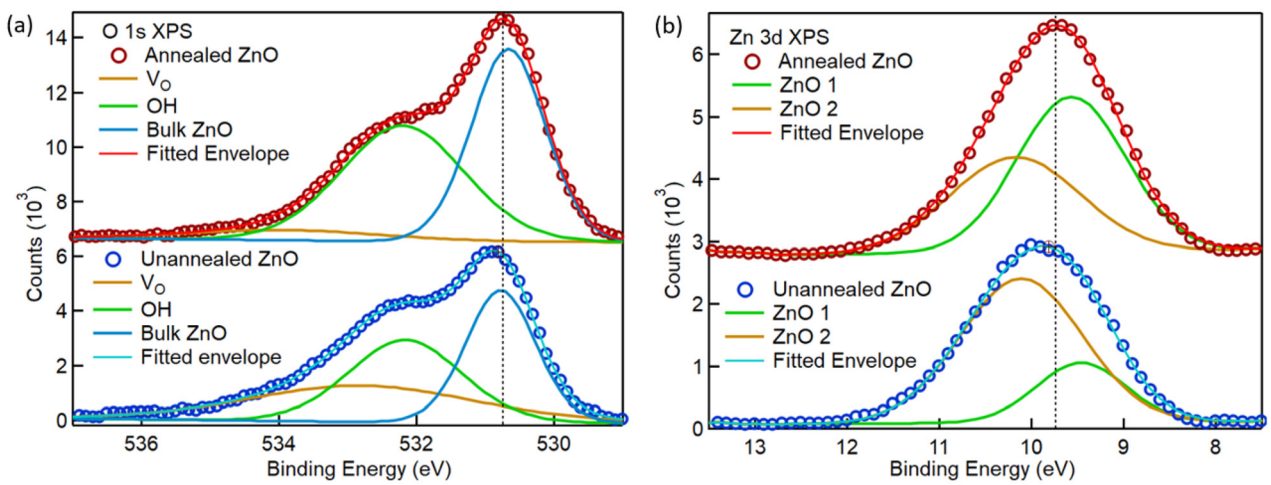

Fig. 2 (a) XPS spectra at the oxygen 1s edge, before (blue open circles, bottom plot) and after annealing (red open circles, top plot), and with fittings to three Gaussian peaks to account for oxygen vacancies (orange solid line), hydroxide surface species (green solid line), and bulk oxygen (teal solid line). The total envelope is shown for each plot (light blue for unannealed ZnO, red for annealed ZnO). (b) The XPS data at the zinc 3d edge, before and after annealing. A fitting with two Gaussian peaks was necessary to reproduce the correct envelope (light blue solid line for unannealed ZnO, red solid line for annealed ZnO).

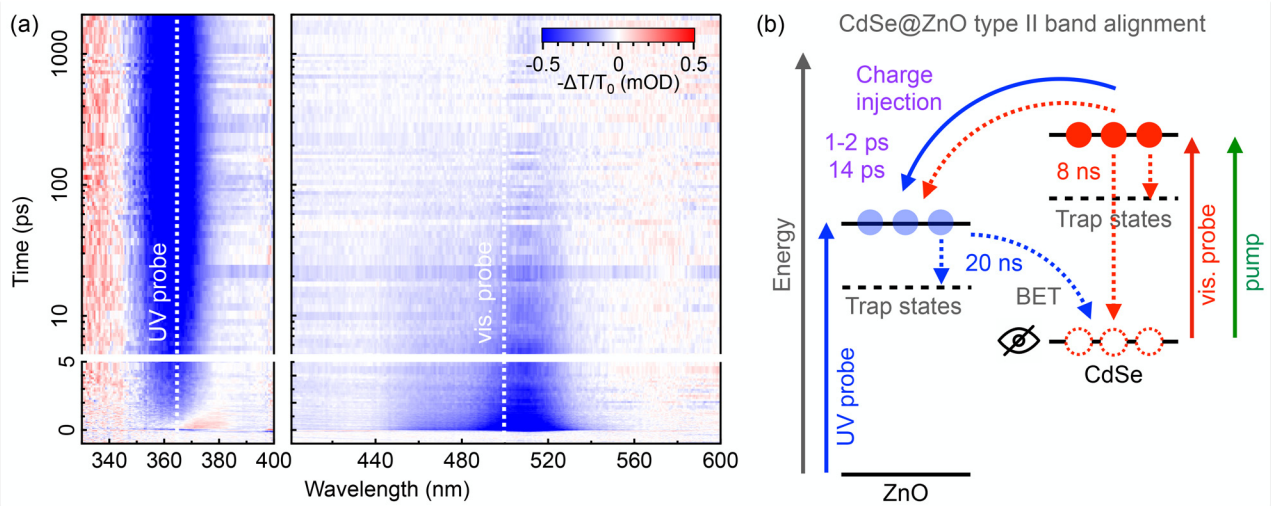

Fig. 3 (a) A typical averaged UV (left) and visible (right) transient absorption data set of CdSe@ZnO excited at 513 nm. The bleach band of the first excitonic peak ~510 nm of the CdSe QDs appears promptly and decays on a tens of ps time scale. The bleach feature of the ZnO nanorods ~360 nm appears within ~1 ps and grows in amplitude over a time scale of ~100 ps. The probing wavelengths (365 nm and 500 nm) for kinetic analysis are indicated by vertical dashed lines. (b) Schematic of the type II band alignment and relaxation pathways of CdSe@ZnO nanorods. The QDs are selectively excited at 513 nm (green arrow). The occupation of the CdSe (red) and ZnO (blue) conduction bands with excited carriers leads to bleach signals in the visible and UV, respectively. Relaxation channels that lead to a decay (dashed arrows) or rise (solid arrows) of electron population are indicated as well. BET = back-electron transfer. Transient spectroscopy in the UV/visible range is not sensitive to holes in the QDs.

duction band. Holes are generally not observed in the transient absorption spectrum of CdSe QDs because of the lower valence band degeneracy and rapid trapping at the surface.[66–68] Insensitivity to the hole population suggests that back-electron transfer of electrons from the ZnO conduction band into the CdSe valence band cannot be observed from the perspective of the CdSe band edge dynamics. Carrier injection from CdSe to ZnO, trapping, and recombination within the CdSe QDs will all lead to a decay of the bleach signal at the first QD excitonic transition.[67,68] Carrier injection into ZnO will result in a bleach signal at the ZnO band gap that grows as the CdSe signal decays.[42] This bleach is due to PSF of injected electrons occupying the ZnO conduction band minimum.

Spectral traces taken at 1 and 100 ps after photoexcitation are shown in Fig. 4a for CdSe@ZnO nanorods in air, and at 1 ps for CdSe QDs with OA ligands in hexane. The transient spectrum of solution-phase CdSe QDs exhibit sharply defined bleach features at the peaks of the first ($1S_e$–$1S_{h_{3/2}}$) and second ($1S_e$–$2S_{h_{3/2}}$) excitonic transitions, with small ESA features at ~535 nm and ~435 nm due to biexcitonic induced red shifts (see Fig. S2† for the full solution-phase transient spectrum).[69,70] At 1 ps, before significant charge transfer has occurred, the CdSe@ZnO spectral trace in the visible resembles the solution-phase CdSe spectrum. Sensitization broadens the CdSe excitonic transitions due to electronic coupling with the ZnO bulk and surface states, obscuring the Stark effect.[71] The second CdSe excitonic transition shares the lowest electron state ($1S_e$) with the first transition, causing it to also be bleached by PSF after band-gap excitation. At 100 ps, charge transfer is nearly completed since the transient bleach in the visible region has decayed nearly to zero while the transient signal in the UV has grown and reached its maximum amplitude.

We note that solution-phase CdSe QDs do not exhibit a significant transient signal in the UV region after 513 nm excitation. Similarly, two-photon excitation of ZnO nanorods with 513 nm does not result in appreciable transient signal at or below the ZnO band gap (S9†). Thus we can use the UV region for specifically probing the dynamics of the MO acceptor moiety and the visible region to specifically probe the dynamics of the CdSe donor moiety of the heterostructure.

The spectral characteristics of both the ZnO and CdSe moieties are the same for the annealed ZnO sample as for the unannealed sample, as shown in Fig. S19.† The similarity is expected for the QDs since they are only impacted by the sensitization, which is identical between samples. For the UV signal, while annealing affects multiple ZnO qualities, the transient UV signal originates from the bulk excitonic transition between valence and conduction bands. The bulk band gap and electron–hole binding energy changes minimally after annealing, and is thus spectrally consistent between ZnO samples.

3.3. Single-wavelength kinetic analysis

Fig. 4b shows representative kinetic traces for CdSe QDs in hexane solution (490 nm, gray circles), and CdSe@ZnO samples in the UV (365 nm, blue circles) and the visible (500 nm, red circles), integrated over a 2 nm bandwidth. Included in Fig. 4b are the fits to a sum-of-exponentials model (for details on the fitting functions and the determination of

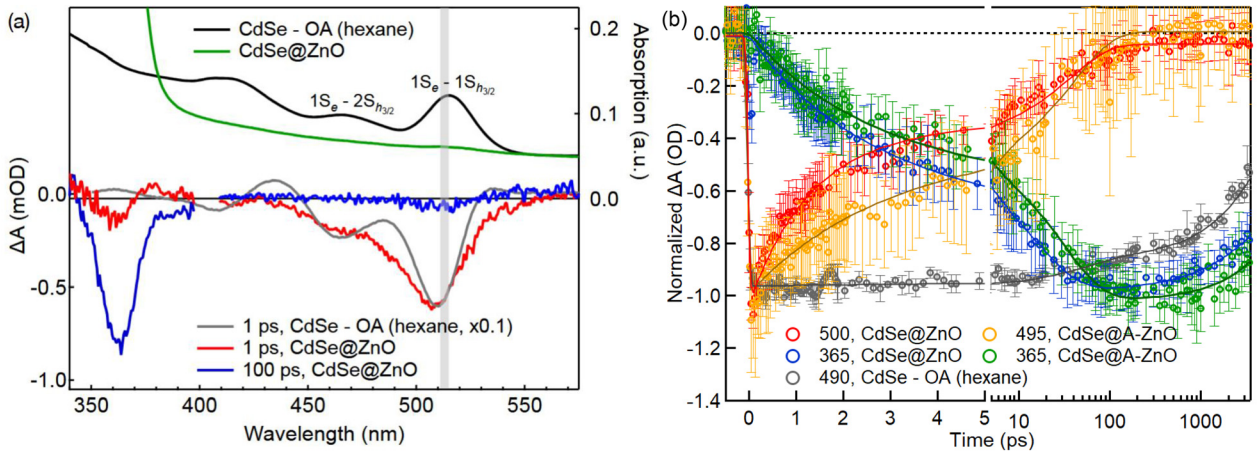

Fig. 4 (a) Transient absorption spectra of CdSe QDs with OA ligands in hexane solution (gray, scaled by a factor of 0.1) at 1 ps, CdSe-sensitized ZnO (CdSe@ZnO) nanorods at 1 ps (red), and at 100 ps (blue) after photoexcitation (all left axis). The spectral bandwidth of the pump light is highlighted with the gray box, centered at 513 nm with 4 nm FWHM. Also shown are the corresponding static UV/visible absorption spectra of CdSe QDs with OA ligands in hexane (black) and CdSe@ZnO nanorods (green) (both right axis, offset for clarity). (b) Representative transient kinetic traces for CdSe QDs with OA ligands in hexane solution at 490 nm (gray), CdSe@ZnO at 500 nm (red circles) and 365 nm (blue circles), and CdSe@A-ZnO at 495 nm (orange circles) and 365 nm (green circles). Solid lines are kinetic fits to the data. The traces are normalized such that their maximum amplitude is set to a value of −1. The error bars represent standard deviations obtained from the average of data sets taken at a single spot. Datasets for all spots are shown in Fig. S10.†

the maximum number of exponentials to include, see S5 and S7†). For CdSe QDs in solution, a sum of two exponential decay functions (with two free parameters each, decay constant τ and amplitude A) is required to fit the kinetics satisfactorily (gray solid curve in Fig. 4b). The first component decays on a time scale of 60 ± 11 ps (relative weight of 11 ± 7%) and the second component on a timescale of 7.9 ± 0.2 ns (89 ± 1%). The first component is assigned to biexciton generation and recombination, which is unavoidable even with low excitation fluence. See S2† for the Poisson distribution of the excitonic population.[5,72] The second component is assigned to single exciton radiative recombination.[69,73]

The transient signal of both CdSe@ZnO samples in the visible decays faster than that of the solution-phase CdSe QDs.[28,32,71] By visual inspection, the amplitude of the ZnO bleach in the UV increases on a similar time scale as the decay of the CdSe signal in the visible, indicating a direct electron transfer pathway from the QDs into ZnO. There is a distinct difference between annealed and unannealed CdSe@ZnO. After annealing ZnO, the kinetics in the visible and UV signals slow down by a factor of ~4. In these measurements a single dataset is insufficient to give statistical certainty, which necessitates collecting multiple datasets and analyzing them in parallel. This allows extracting time constants and amplitudes that are representative of the whole sample. Note that the bottom axis becomes logarithmic after 5 ps.

Quantitatively, the QD-specific kinetics at 500 nm are fitted with a sum of three exponential decay functions, one of which is a fixed long decay component representing carrier population decaying outside of the fitting window (5.5 ns), which is held at the recombination constant of the solution phase CdSe (7.9 ns). ZnO-specific kinetics at 365 nm were fitted with two rising exponentials and a single-exponential decay function with an amplitude equal to the negative sum of the amplitudes of the rising exponentials. This choice of amplitude for the decay function allows us to extract a realistic time constant, assuming that the signal decays back to zero outside the fitting window. The fits are shown alongside the kinetic traces in Fig. 4b (solid curves), and the fitted time constants and amplitudes (resulting from averaging the fitted values of measurements at different sample positions) are recorded in Table 1. An overview of fitted time constants and amplitudes for all sample positions is given in S7.†

The similarity of the τ_1 and τ_2 decay/rise constants and their relative amplitudes in the respective CdSe and ZnO moieties in CdSe@ZnO and CdSe@A-ZnO prompts us to relate these kinetic pathways to each other. In CdSe@ZnO, τ_1 is slightly longer for ZnO (1.8 ± 0.3 ps rise) compared to CdSe (0.8 ± 0.1 ps decay), while the τ_2 values overlap within errors (13 ± 3 ps rise and 15 ± 3 ps decay for ZnO and CdSe, respectively). Importantly, the relative amplitudes for τ_1 and τ_2 are the same for both moieties, within error. Since PSF by excited electrons is the primary contribution to the transient signal at the two band edges, the relative contribution and decay time of each exponential component is a good measure of the movement of electron population across the CdSe/ZnO interface. Each material has a different PSF amplitude per carrier due to their different band curvatures and degeneracies, thus only relative (normalized) amplitudes are directly comparable.

CdSe@A-ZnO shows similar behavior between visible and UV kinetics with a few important differences. τ_1 and τ_2 values

Table 1 Averaged fitted time constants and relative normalized amplitudes (in parentheses) obtained from fitting the kinetic traces at 490 nm (CdSe with OA ligands in hexane), 500 nm (CdSe in CdSe@ZnO) and 365 nm (ZnO in CdSe@ZnO) to a sum-of-exponentials model. τ_1 and τ_2 are the first two rising/decaying time constants for ZnO/CdSe in CdSe@ZnO, respectively. τ_{EX} is the decay constant assigned to biexcitonic decay in solution-phase CdSe QDs. τ_R is the decay constant assigned to the recombination of carriers in CdSe (fixed for the CdSe in CdSe@ZnO and CdSe@A-ZnO fit). τ_{BET} is the fitted decay constant of the ZnO signal assigned to back electron transfer (BET). The relative amplitude of the latter was constrained to be equal to the negative sum of the two rising components

Wavelength	τ_1	τ_2	τ_{EX}	τ_R	τ_{BET}
490 nm (CdSe in hexane)	—	—	60 ± 11 ps (11 ± 7%)	7.9 ± 0.2 ns (89 ± 1%)	—
500 nm (CdSe in CdSe@ZnO)	0.8 ± 0.1 ps (56 ± 4%)	15 ± 3 ps (40 ± 4%)	—	7.9 ns (4 ± 1%)	—
365 nm (ZnO in CdSe@ZnO)	1.8 ± 0.3 ps (48 ± 9%)	13 ± 3 ps (52 ± 8%)	—	—	17 ± 1 ns (−100%)
500 nm (CdSe in CdSe@A-ZnO)	2.5 ± 0.6 ps (43 ± 5%)	53 ± 11 ps (48 ± 3%)	—	7.9 ns (8 ± 6%)	—
365 nm (ZnO in CdSe@A-ZnO)	3.4 ± 0.5 ps (41 ± 4%)	47 ± 6 ps (59 ± 3%)	—	—	26 ± 2 ns (−100%)

have increased significantly after annealing. τ_1 has increased by almost 1.5 ps for CdSe (to 2.5 ± 0.6 ps) and ZnO (3.4 ± 0.5 ps), and τ_2 has increased by nearly 40 ps (CdSe 53 ± 11 ps, ZnO 47 ± 6 ps), and is identical between ZnO and CdSe within the error bars. The amplitudes after annealing are again in good agreement, with τ_1 being weighted slightly less than τ_2. These results can be interpreted clearly in Fig. 4; annealing has slowed down the charge injection timescale significantly, and increased the separation between them.

Biexcitonic decay of solution phase OA-CdSe was measured to be 60 ± 11 ps, and only accounted for 10% of the amplitude. CdSe in the QDH has a similar excited state population, but the dynamics take place on a much faster time scale than the biexcitonic decay and accounts for a much greater portion of the carrier population. Due to this, any biexcitonic states would rapidly depopulate, and biexcitonic decay can be excluded from the interpretation of the CdSe dynamics in the sensitized CdSe@ZnO. This is true for CdSe@A-ZnO as well, even though τ_2 corresponds much more closely with solution phase biexcitonic decay of CdSe. The reasoning is that any biexcitonic state would decay very rapidly from τ_1 due to charge injection. In addition, this is plausible for CdSe kinetics, but not for the measured kinetics in ZnO, which will be examined in detail in section 3.4.

CdSe@ZnO nanorod heterostructures show bimodal interfacial charge injection on two distinct time scales: $\tau_1 \sim$ 1–2 ps and $\tau_2 \sim$ 14 ps (Fig. 3b). The slow decay components are attributed to carrier recombination (τ_R for CdSe), back-electron transfer (BET, τ_{BET} for ZnO) and/or carrier trapping in defect states.[28,40,71,74] CdSe@A-ZnO preserves this bimodal charge injection and further distinguishes the timescales: $\tau_1 \sim$ 2–3 ps and $\tau_2 \sim$ 50 ps. We emphasize that the fast decay of CdSe QDs in QD materials has often been assigned to carrier trapping using techniques that probe CdSe selectively.[28,40,71] Here we show that this decay can indeed correspond to charge injection by matching the QD decay components to the corresponding carrier rise signals in the ZnO moiety. Annealed ZnO slows down τ_1 of the CdSe and brings it close to agreement with τ_1 of A-ZnO, showing that the fast decay could be attributed to direct charge injection or trapping at defect-derived sub-band gap states of ZnO. A dual probe technique assessing the dynamics from the donor and acceptor viewpoints is thus prerequisite to obtain a holistic picture of the interfacial carrier transport.

3.4. Origin of bimodal interfacial charge transfer

Multiexponential rise times upon carrier injection in ZnO have been observed in dye-sensitized ZnO nanoparticles by time-resolved THz and IR spectroscopy, with similar timescales and amplitudes as in this study.[23,33,75,76] Those dynamics have been attributed to the interaction of the cationic dye and injected electrons forming an interfacial charge-transfer state that dissociates on the 10's of ps timescale. Previous results with transient absorption and THz spectroscopy on CdSe-sensitized ZnO nanorods in particular have attributed the fastest CdSe decay (1–3 ps) to formation of a charge-transfer state (CTS), followed by dissociation of this state to give a prolonged growth of free carrier conductivity in ZnO over 20 to 60 ps.[28,29] CTS's are likely formed from sub-band gap surface states in the metal oxide, thus a bound interfacial state is not expected to contribute to the bleach of the band edge transition in ZnO due to the electron not occupying the bulk DOS.[23,25,77] In the CdSe@ZnO and in supporting measurements on dye-sensitized ZnO, there is no spectral signal with kinetics to match the rapidly populated CTS, confirming that there is no overlap between this transition and the band edge ZnO or CdSe transitions (see S10†).[25,42,60,78] The kinetics of the CTS population are not directly measured here.

Based on these considerations, we propose various scenarios to explain the bimodal kinetics in the CdSe@ZnO heterostructures: (i) a ps charge transfer pathway from CdSe into an intermediate CTS with dissociation occurring on a fast (τ_1) and a slow (τ_2) timescale; or (ii) a ps (τ_1) charge transfer pathway from CdSe into ZnO and subsequent carrier cooling of injected electrons in ZnO on the tens of ps (τ_2) time scale; or (iii) charge transfer from QD populations with different driving forces and therefore different charge injection time scales.

Scenarios (i) and (ii) would attribute only τ_1 in CdSe to charge injection, which leaves τ_2 open to interpretation, while also ruling out biexcitonic decay. The fact that τ_2 of CdSe is similar in both time constant and amplitude to the τ_2 rise

component in the ZnO moiety would then be a coincidence, and necessitate an exotic and unlikely explanation for the biexponential rise of the total ZnO signal (*e.g.* a sequential dissociation from an optically dark state, with varying spectral weight in the conduction band). Scenario (ii) is discarded since carrier cooling in ZnO takes place within a ps from high-lying states and is accompanied by spectral changes from band-gap renormalization that are not observed in the present case, and does not explain the impact of annealing on the charge transfer timescales.[65] In addition, the amount of two-photon absorption that would lead to excess carrier energy and significant carrier cooling is estimated to be at most 1% under the excitation conditions of the present experiment (S9†). The closely matched time constants and relative weights in the kinetic fits of the CdSe and ZnO moieties in CdSe@ZnO (and A-ZnO) make it more likely that the measured kinetics are due to electron transfer from two different states with independent driving forces (scenario (iii)).

The relative concentration of the charge transfer states in scenario (iii) indicates that they are non-interacting. If the fastest charge injection pathway was accessible by all QDs, then charge injection would proceed through that pathway with an efficiency governed by the ratio between the two timescales. For CdSe@ZnO, the measured injection timescales would give $1-\frac{\tau_1}{\tau_1+\tau_2}\approx 85-95\%$ of charge injection proceeding on the fast timescale (0.8–1.8 ps) if it was available for all QDs, which disagrees with the relative amplitudes of τ_1 and τ_2 (~50%). This relationship is preserved after annealing: ~94% of charge injection would proceed through the fast pathway for CdSe@A-ZnO. This points to a heterogeneous mechanism of non-interacting states being responsible for the bimodal charge injection dynamics. A single population of charge injectors with a distribution of charge transfer rates was also considered using the stretched exponential function. However, this does not improve the best fit statistics and does not give a physically meaningful distribution (S5†).[79]

The first source of heterogeneity may be in QD size or QD–ZnO attachment, which could result in different charge transfer driving forces.[28,80] The QD size dispersion is relatively small (±0.1 nm, S8†) and the pump beam at 513 nm predominately excites QDs with the mean diameter of 2.6 nm (Fig. 4a) which results in a narrow range of driving forces for excited QDs, in contrast to the observed disparate τ_1 and τ_2 injection timescales. Different driving forces may also result from directly and indirectly attached QDs (*i.e.* QDs that are not in direct contact with the ZnO surface, but rather aggregated with other QDs).[28] Such an indirect attachment is expected to result in charge transfer into ZnO on a longer timescale. However, the QD coverage is estimated at 8% and 12% of a monolayer for ZnO and A-ZnO respectively (S8†), and approximately 1 in 5 QDs are excited (S2†). The dilute excitation conditions and low QD loading is critical to limiting inter-QD coupling and the aggregate concentration. However aggregates cannot be fully excluded. Excitonic diffusion within an aggregate will have some initial rapid diffusion that is partially governed by the inhomogeneous linewidth broadening within the aggregate, but is dependent on the ligand coverage and excitation conditions. Whether the exciton is in contact with the interface on the sub-nanosecond timescale cannot be predicted based on the limited information available.[81,82] Given this, the statistical likelihood of having half of all charge transfer taking place from indirectly attached QDs is small. This is shown in S11† where a spin-coated CdSe@ZnO sample shows significantly faster trapping of charges without any charge injection. Additionally, the concentration of QD aggregates is similar between CdSe@ZnO and CdSe@A-ZnO due to the identical sensitization conditions, and does not explain why the charge injection timescale is impacted so strongly. While these are strong points, a global kinetic model based on heterogeneous injection was still considered and tested, with the results shown in S12.† This model was unable to replicate the measured kinetics.

Finally, the two possible binding motifs (carboxylic acid and thiol) of the MPA linker molecule could induce different surface energetics.[80] The thiol is much more likely to coordinate to the CdSe than the carboxylic acid,[83,84] and due to the step-wise ligand exchange and phase transfer of CdSe, the amount of excess ligand during sensitization is limited, preserving the thiol coordinated to CdSe and carboxylate to ZnO. Since each QD is likely adsorbed to the ZnO nanorods through multiple ligands, mono- *vs.* bidentate coordination is unlikely to contribute to the two distinct charge transfer timescales. We conclude that heterogeneity from the electron-donating CdSe (derived from size distribution, QD aggregates, or binding-ligands) is unlikely to be responsible for the bimodal charge injection.

Charge injection time scales into MO nanomaterials have previously been shown to be influenced by the electronic structure of the conduction band of the MO and the coupling between the electron donor (dye or QD) to the interface.[85] In particular, band bending, *i.e.* the local curving of the electronic band structure near an interface or junction, can modulate the driving force for interfacial charge injection.[18,86] Such band bending effects in ZnO are sizable and have been related to the photocatalytic activity of ZnO-based materials.[19,60] The low static dielectric constant of ZnO relative to other MOs allows for strong band bending effects near the surface even in small nanoparticles with diameters of 10 nm, and has been credited for charge injection differences between dye-sensitized ZnO and TiO_2.[21,87] The extent of band bending depends on the crystal facet.[17,58] In the present work, we propose that the bimodal interfacial charge transfer dynamics originates from injection at different facets of the ZnO nanorods: the (0001) facets at the top of the nanorods and the $(10\bar{1}0)$ facets at the side of the nanorods (Fig. 1), with downward band bending magnitudes of ~−580 meV (large driving force, fast injection pathway) and ~−300 meV (small driving source, slow injection pathway), respectively (Fig. 6).[17] A-ZnO would then have reduced band bending magnitudes for the two facets and altered driving forces,

based on the XPS results shown here and in previous works.[19,60] The two facets have adsorbates that chemisorb with varying strength, resulting in different degrees of band bending at the different facets for this annealing temperature (400 °C).[17,19] The relative amplitudes of the charge injections pathways then depend on the QD coverage of the respective facets. While there is much more surface area for the $(10\bar{1}0)$ facets, the ZnO (0001) facets have a higher adsorption rate of CdSe QDs.[55] In addition, the available sensitization area may be limited due to the close packing of nanorods and the inability of the QD solution to permeate the entire ZnO nanorod sample.

This bimodal charge injection is further preserved when different sizes of QDs are used to sensitize ZnO. Fig. 5 shows the aggregate charge injection rates $(1/\tau)$ of all samples, and in depth in S12† including the raw results and fittings. The 2.3 nm CdSe QD samples were not globally fit using the model from 3.5 due to non-negligible two-photon absorption, which has kinetics that overlap significantly with the fast charge transfer timescale. The rates were instead used from multi-exponential fittings and shown in S7.† 2.3 nm CdSe@ZnO had charge injection rates of 1 ± 0.24 ps^{-1} and 0.04 ± 0.012 ps^{-1}, and 0.6 ± 0.04 ps^{-1} and 0.017 ± 0.001 ps^{-1} for 4.2 nm CdSe@ZnO. The 2.6 nm CdSe for annealed and unannealed ZnO shows the rates extracted from global fitting, as reported in section 3.5. All sizes showed bimodal charge injection, with the largest QDs having the widest separation in timescales. Notably annealing ZnO renders the energetic landscape of 2.6 nm CdSe@A-ZnO nearly equivalent to that of 4.2 nm CdSe@ZnO. The other striking feature of these results is the ultrafast charge transfer for all CdSe sizes. Previous reports have primarily considered charge injection on timescales $\approx\tau_2$, while these result show unequivocally that the energetic landscape of sensitized ZnO has an even faster component, and cannot be reduced to a single pathway.[23,33,75,76]

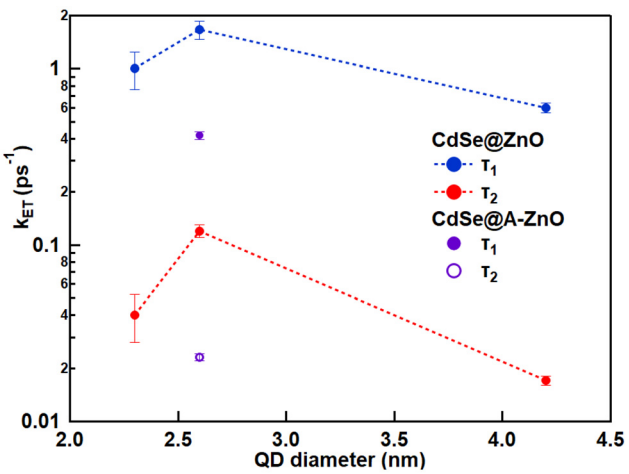

Fig. 5 Aggregate charge transfer rates from sensitized ZnO with 2.3 nm, 2.6 nm, and 4.2 nm CdSe QDs. Two rate constants were extracted from each system. 2.3 nm CdSe@ZnO was fit to a sum of exponentials model, while the 2.6 nm, 2.6 nm CdSe@A-ZnO, and 4.2 nm systems were globally fit using the model reported in the main text.

3.5. Optically dark intermediate state and global target analysis

Having established the bimodal charge injection mechanism in CdSe@ZnO, we now take a closer look at the fast injection pathway, characterized by τ_1 (Table 1). The τ_1 decay time constant in the CdSe moiety (τ_1 = 0.8 ± 0.1 ps @ZnO, and 2.5 ± 0.1 ps @A-ZnO) is shorter than the τ_1 rise time constant in the ZnO moiety (τ_1 = 1.8 ± 0.3 ps, and 3.4 ± 0.5 ps for A-ZnO), meaning that the electron transfer out of the CdSe QDs is faster than the arrival of injected electrons into the bulk conduction band of the ZnO nanorods. Based on our rigorous sampling strategy to average out variations in dynamics due to the macroscopic heterogeneity of the sample (S6†), we believe that the standard deviations of these fitted time constants are a realistic measure of uncertainty and that the differences in τ_1 for the donor and acceptor moieties are statistically significant. We attribute this difference in time constants to the existence of an optically dark intermediate state, *i.e.* a state in which injected electrons get trapped before diffusing into the MO bulk. Such states, localized at the surface of nanoparticles, often do not exhibit appreciable absorption in the UV-Visible region due to their low density and red-shifted indirect transition energies.[26,88] The absence of this state for τ_2, where the charge injection values overlap very clearly, could be due to effects that reduce the coupling between interfacial carriers, or an inability to resolve an intermediate state with a short lifetime. The coulombic interaction could be screened due to the dielectric environment of ZnO, or image charge effects of the bare hole in CdSe.

Based on the above considerations, we conducted a global target fit analysis using a four-state kinetic model depicted in Fig. 6. This global fitting allows the amplitudes of CdSe and

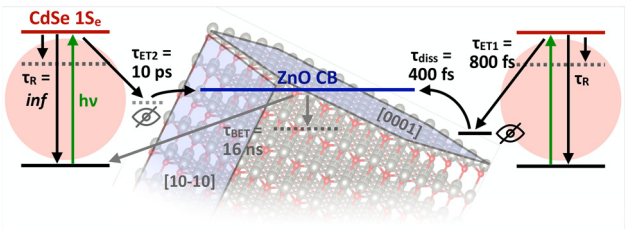

Fig. 6 Proposed bimodal interfacial charge injection pathways in CdSe@ZnO nanorod heterostructures (τ_{ET1} and τ_{ET2}). Charge injection takes place through two independent acceptor states with different driving forces imposed by band bending at different ZnO crystal facets. Trapping in an optically dark intermediate state is inferred for the fast injection pathway (τ_{ET1}), followed by dissociation (τ_{diss}) into the ZnO bulk DOS probed in the UV region of the spectrum. Charge recombination and/or trapping in the QD and ZnO moieties are represented by τ_R (fixed to a large value) and τ_{BET}, respectively. The time constants are obtained from a global target fit analysis.

ZnO to vary independently of each other, and with normalized amplitudes because the measurements are not taken within a single spectral window. Thus quantum yield of each charge injection pathway could not be determined absolutely. The bimodal charge transfer behavior is taken into account with two decay processes in the CdSe moiety described by time constants τ_{ET1} and τ_{ET2}, which were fitted to 0.8 ± 0.1 ps and 10 ± 1 ps for CdSe@ZnO. To account for the slower rise time of the ZnO bleach feature, we define a new time constant, τ_{diss}, that describes the dissociation/depopulation of the optically dark intermediate state and arrival of electrons in the ZnO conduction band on the 0.4 ± 0.1 ps timescale. The 10 ps population decay in the QDs and the corresponding rise of population in the ZnO conduction band are both described by time constant τ_{ET2} – an intermediate state could not be resolved for this injection pathway. This same fitting was applied to CdSe@A-ZnO, which showed τ_{ET1} of 2.4 ± 0.1 ps, and τ_{ET2} was fit to 44 ± 2 ps. However τ_{diss} could not be resolved or is non-existent (~0 ± 0.1 ps) in this sample. It should be considered whether this intermediate state can also be attributed to localization near the surface from intrinsic surface potentials of strong band bending, as has been seen in dye-sensitized systems on the 100's of ps timescale.[60] The fitted time constants for this kinetic model and both samples are shown in Fig. 6. These results show that before annealing approximately half of the QDs transfer charge within 800 fs to an optically dark state, while the other half transfers charge within 10 ps directly to the ZnO conduction band. The optically dark state dissociates 400 fs after being populated. Annealing separates the two timescales dramatically to 2.4 ps and 44 ps, without an observable dark state. Such a direct accounting of the excited carrier population is only possible when both the donor and acceptor moieties can be measured with specificity and within a single technique. In the ESI S12† we explore different kinetic models, including a heterogeneous QD model where the CdSe populations are not distinct. This model tests whether aggregates can explain the shape of the signal in ZnO, but the single, shared population of CdSe QDs leads to distorted kinetics and poor fittings are seen in ZnO. The global target analysis based on the four-state model of Fig. 6 provides the best fit to the data.

4. Conclusion

In this contribution, we show that broadband transient absorption spectroscopy spanning the UV and visible regions is a powerful tool to correlate the dynamics of the electron-donating and -accepting moieties of photoexcited heterostructured nanomaterials. Previous studies focusing on probing the dynamics of a single moiety, or using different probing spectroscopies, suffer from inconsistencies in reported time scales and reproducibility challenges.[40,47,71] In the present work, we use a single spectroscopic technique applied in combination with a rigorous sampling strategy to average out macroscopic heterogeneities and a global fit analysis encompassing both the electron donor and acceptor dynamics. This suggests a bimodal charge injection mechanism for CdSe QD-sensitized ZnO nanorods based on heterogeneous acceptor states: a fast (<1 ps) indirect charge injection pathway that involves the population of an optically dark intermediate state, and a direct charge injection pathway on the tens of ps time scale without an observable intermediate state. These timescales were strongly impacted by a simple annealing of the ZnO, which pushed charge injection to 2.4 ps and 44 ps for the fast and slow injection pathways. We propose that different band bending energetics at the facets of the ZnO nanorods are responsible for the bimodal kinetics and the formation of the intermediate state. This effort opens opportunities for future investigation into the formation of these critical intermediate states of QDHs, as well as allowing systematic studies of metal oxide characteristics, such as varying the defect concentration or aspect ratio of ZnO nanostructures.

Author contributions

R. M. V. and C. P. D conceived and designed the project. C. P. D. and M. J. E. prepared the samples. C. P. D. and T. C. R. carried out the experiments. R. M. V., C. P. D., T. C. R. and J. V. W. interpreted the data. C. P. D. and R. M. V. wrote the manuscript. All the authors commented on the manuscript.

Conflicts of interest

There are no conflicts to declare.

Data availability

The code for bulk analysis of OTA data can be found at **https://github.com/BozarkV2/TA_analysis**, while the raw data can be provided upon request.

Acknowledgements

This material is based upon work supported by the U.S. Department of Energy, Office of Science, Solar Photochemistry under award no. DE-SC0021062. RMV acknowledges funding by the Initiative and Networking Fund of the Helmholtz Association. MJE acknowledges funding by the Photonics at Thermodynamic Limits Energy Frontier Research Center funded by the U.S. Department of Energy, Office of Science and Office of Basic Energy Sciences under Award Number DE-SC0019140 and the National Science Foundation under Grant No. [2418864].

References

1 F. Rehman, I. H. Syed, S. Khanam, S. Ijaz, H. Mehmood, M. Zubair, Y. Massoud and M. Q. Mehmood, *Energy Adv.*, 2023, **2**, 1239–1262.
2 I. Mora-Seró, *Adv. Energy Mater.*, 2020, **10**, 2001774.
3 R. S. Selinsky, Q. Ding, M. S. Faber, J. C. Wright and S. Jin, *Chem. Soc. Rev.*, 2013, **42**, 2963–2985.
4 V. I. Klimov, A. A. Mikhailovsky, D. W. McBranch, C. A. Leatherdale and M. G. Bawendi, *Science*, 2000, **287**, 1011–1013.
5 V. I. Klimov, J. A. McGuire, R. D. Schaller and V. I. Rupasov, *Phys. Rev. B: Condens. Matter Mater. Phys.*, 2008, **77**, 195324.
6 M. S. Kirschner, D. C. Hannah, B. T. Diroll, X. Zhang, M. J. Wagner, D. Hayes, A. Y. Chang, C. E. Rowland, C. M. Lethiec, G. C. Schatz, L. X. Chen and R. D. Schaller, *Nano Lett.*, 2017, **17**, 5314–5320.
7 A. J. Nozik, M. C. Beard, J. M. Luther, M. Law, R. J. Ellingson and J. C. Johnson, *Chem. Rev.*, 2010, **110**, 6873–6890.
8 J. B. Sambur, T. Novet and B. A. Parkinson, *Science*, 2010, **330**, 63–66.
9 G. S. Selopal, H. Zhao, Z. M. Wang and F. Rosei, *Adv. Funct. Mater.*, 2020, **30**, 1908762.
10 S. Mariotti, E. Köhnen, F. Scheler, K. Sveinbjörnsson, L. Zimmermann, M. Piot, F. Yang, B. Li, J. Warby, A. Musiienko, D. Menzel, F. Lang, S. Keßler, I. Levine, D. Mantione, A. Al-Ashouri, M. S. Härtel, K. Xu, A. Cruz, J. Kurpiers, P. Wagner, H. Köbler, J. Li, A. Magomedov, D. Mecerreyes, E. Unger, A. Abate, M. Stolterfoht, B. Stannowski, R. Schlatmann, L. Korte and S. Albrecht, *Science*, 2023, **381**, 63–69.
11 B. A. Gregg, *J. Phys. Chem. B*, 2003, **107**, 4688–4698.
12 J. Fan, Y. Hao, C. Munuera, M. García-Hernández, F. Güell, E. M. Johansson, G. Boschloo, A. Hagfeldt and A. Cabot, *J. Phys. Chem. C*, 2013, **117**, 16349–16356.
13 T. P. Chou, Q. Zhang and G. Cao, *J. Phys. Chem. C*, 2007, **111**, 18804–18811.
14 C. S. Ponseca, P. Chábera, J. Uhlig, P. Persson and V. Sundström, *Chem. Rev.*, 2017, **117**, 10940–11024.
15 M. Y. Guo, A. M. C. Ng, F. Liu, A. B. Djurišić, W. K. Chan, H. Su and K. S. Wong, *J. Phys. Chem. C*, 2011, **115**, 11095–11101.
16 M. Law, L. E. Greene, J. C. Johnson, R. Saykally and P. Yang, *Nat. Mater.*, 2005, **4**, 455–459.
17 R. Heinhold, S. P. Cooil, D. A. Evans and M. W. Allen, *J. Phys. Chem. C*, 2014, **118**, 24575–24582.
18 Z. Zhang and J. T. Yates, *Chem. Rev.*, 2012, **112**, 5520–5551.
19 J. Mahl, O. Gessner, J. V. Barth, P. Feulner and S. Neppl, *ACS Appl. Nano Mater.*, 2021, **4**, 12213–12221.
20 V. Consonni, J. Briscoe, E. Kärber, X. Li and T. Cossuet, *Nanotechnology*, 2019, **30**, 362001.
21 U. Ozgur, Y. I. Alivov, C. Liu, A. Teke, M. A. Reshchikov, S. Doğan, V. Avrutin, S.-J. Cho and H. Morkoç, *J. Appl. Phys.*, 2005, **98**, 041301.
22 H. Wei, J.-W. Luo, S.-S. Li and L.-W. Wang, *J. Am. Chem. Soc.*, 2016, **138**, 8165–8174.
23 D. Stockwell, Y. Yang, J. Huang, C. Anfuso, Z. Huang and T. Lian, *J. Phys. Chem. C*, 2010, **114**, 6560–6566.
24 K. Virkki, E. Tervola, M. Ince, T. Torres and N. V. Tkachenko, *R. Soc. Open Sci.*, 2018, **5**, 180323.
25 H. Němec, J. Rochford, O. Taratula, E. Galoppini, P. Kužel, T. Polívka, A. Yartsev and V. Sundström, *Phys. Rev. Lett.*, 2010, **104**, 197401.
26 F. Piersimoni, R. Schlesinger, J. Benduhn, D. Spoltore, S. Reiter, I. Lange, N. Koch, K. Vandewal and D. Neher, *J. Phys. Chem. Lett.*, 2015, **6**, 500–504.
27 U. Hörmann, S. Zeiske, F. Piersimoni, L. Hoffmann, R. Schlesinger, N. Koch, T. Riedl, D. Andrienko and D. Neher, *Phys. Rev. B*, 2018, **98**, 155312.
28 K. Žídek, K. Zheng, C. S. Ponseca, M. E. Messing, L. R. Wallenberg, P. Chábera, M. Abdellah, V. Sundström and T. Pullerits, *J. Am. Chem. Soc.*, 2012, **134**, 12110–12117.
29 S. B. N. , H. Němec, K. Žídek, M. Abdellah, M. J. Al-Marri, P. Chábera, C. Ponseca, K. Zheng and T. Pullerits, *Phys. Chem. Chem. Phys.*, 2017, **19**, 6006–6012.
30 K. J. Schnitzenbaumer and G. Dukovic, *Nano Lett.*, 2018, **18**, 3667–3674.
31 H. Zhu, Y. Yang, K. Wu and T. Lian, *Annu. Rev. Phys. Chem.*, 2016, **67**, 259–281.
32 M. Abdellah, K. Žídek, K. Zheng, P. Chábera, M. E. Messing and T. Pullerits, *J. Phys. Chem. Lett.*, 2013, **4**, 1760–1765.
33 A. Furube, R. Katoh, T. Yoshihara, K. Hara, S. Murata, H. Arakawa and M. Tachiya, *J. Phys. Chem. B*, 2004, **108**, 12583–12592.
34 S. Lian, J. A. Christensen, M. S. Kodaimati, C. R. Rogers, M. R. Wasielewski and E. A. Weiss, *J. Phys. Chem. C*, 2019, **123**, 5923–5930.
35 A. Honarfar, H. Mourad, W. Lin, A. Polukeev, A. Rahaman, M. Abdellah, P. Chábera, G. Pankratova, L. Gorton, K. Zheng and T. Pullerits, *ACS Appl. Energy Mater.*, 2020, **3**, 12525–12531.
36 M. M. Taheri, K. C. Elbert, S. Yang, B. T. Diroll, J. Park, C. B. Murray and J. B. Baxter, *J. Phys. Chem. C*, 2021, **125**, 31–41.
37 K. B. Ucer, R. A. Wall, K. C. Lipke and R. T. Williams, *Phys. Status Solidi B*, 2008, **245**, 2680–2683.
38 J. B. Asbury, Y. Q. Wang and T. Lian, *J. Phys. Chem. B*, 1999, **103**, 6643–6647.
39 J. J. H. Pijpers, R. Koole, W. H. Evers, A. J. Houtepen, S. Boehme, C. de Mello Donegá, D. Vanmaekelbergh and M. Bonn, *J. Phys. Chem. C*, 2010, **114**, 18866–18873.
40 K. Žídek, K. Zheng, M. Abdellah, P. Chábera, T. Pullerits and M. Tachyia, *J. Phys. Chem. C*, 2014, **118**, 27567–27573.
41 T. Hansen, K. Žídek, K. Zheng, M. Abdellah, P. Chábera, P. Persson and T. Pullerits, *J. Phys. Chem. Lett.*, 2014, **5**, 1157–1162.
42 E. Baldini, T. Palmieri, T. Rossi, M. Oppermann, E. Pomarico, G. Auböck and M. Chergui, *J. Am. Chem. Soc.*, 2017, **139**, 11584–11589.
43 L. Vayssieres, *Adv. Mater.*, 2003, **15**, 464–466.

44 R. S. Kammel and R. S. Sabry, *J. Sci.: Adv. Mater. Devices*, 2019, **4**, 420–424.
45 J. B. Baxter, A. M. Walker, K. V. Ommering and E. S. Aydil, *Nanotechnology*, 2006, **17**, DOI: 10.1088/0957-4484/17/11/S13.
46 S.-W. Han, H.-J. Yoo, S. J. An, J. Yoo and G.-C. Yi, *Appl. Phys. Lett.*, 2005, **86**, 021917.
47 M. Albaladejo-Siguan, E. C. Baird, D. Becker-Koch, Y. Li, A. L. Rogach and Y. Vaynzof, *Adv. Energy Mater.*, 2021, **11**, 2003457.
48 R. I. Shrager and R. W. Hendler, *J. Biochem. Biophys. Methods*, 1998, **36**, 157–173.
49 R. Hyndman and G. Athanasopoulos, *Forecasting: Principles and Practice*, Otexts, 3rd edn, 2021.
50 J. Jasieniak, L. Smith, J. van Embden, P. Mulvaney and M. Califano, *J. Phys. Chem. C*, 2009, **113**, 19468–19474.
51 F. Urbach, *Phys. Rev.*, 1953, **92**, 1324.
52 O. Herrfurth, S. Richter, M. Rebarz, S. Espinoza, J. Zúñiga-Pérez, C. Deparis, J. Leveillee, A. Schleife, M. Grundmann, J. Andreasson and R. Schmidt-Grund, *Phys. Rev. Res.*, 2021, **3**, 013246.
53 E. A. Dalchiele, C. J. Pereyra, D. Ariosa, R. Henríquez, L. Campo, E. Muñoz, F. Martín, E. Navarrete-Astorga, R. Romero, J. R. Ramos-Barrado, R. E. Marotti and A. Cuevas, *Opt. Lett.*, 2021, **46**, 2360–2363.
54 T. Toyoda, W. Yindeesuk, K. Kamiyama, K. Katayama, H. Kobayashi, S. Hayase and Q. Shen, *J. Phys. Chem. C*, 2016, **120**, 2047–2057.
55 T. Toyoda, W. Yindeesuk, K. Kamiyama, S. Hayase and Q. Shen, *J. Phys. Chem. C*, 2016, **120**, 16367–16376.
56 T. Toyoda, Q. Shen, N. Nakazawa, Y. Yoshihara, K. Kamiyama and S. Hayase, *Mater. Res. Express*, 2022, **9**, 025005.
57 E. Tosi, D. Comedi and G. Zampieri, *Appl. Surf. Sci.*, 2019, **495**, 143592.
58 D. Mora-Fonz, J. Buckeridge, A. J. Logsdail, D. O. Scanlon, A. A. Sokol, S. Woodley and C. R. A. Catlow, *J. Phys. Chem. C*, 2015, **119**, 11598–11611.
59 W. S. Silva, C. Stiehler, E. A. Soares, E. M. Bittar, J. C. Cezar, H. Kuhlenbeck, H. J. Freund, E. Cisternas and F. Stavale, *Phys. Rev. B*, 2018, **98**, 155416.
60 S. Neppl, J. Mahl, F. Roth, G. Mercurio, G. Zeng, F. M. Toma, N. Huse, P. Feulner and O. Gessner, *J. Phys. Chem. Lett.*, 2021, **12**, 11951–11959.
61 J. Fang, H. Fan, Y. Ma, Z. Wang and Q. Chang, *Appl. Surf. Sci.*, 2015, **332**, 47–54.
62 C. J. Barnett, J. D. McGettrick, V. S. Gangoli, J. Navarro-Torres, T. Watson, T. G. Maffeis, A. R. Barron and A. O. White, *Mater. Lett.*, 2021, **301**, 130288.
63 B. Carlson, K. Leschkies, E. S. Aydil and X.-Y. Zhu, *J. Phys. Chem. C*, 2008, **112**, 8419–8423.
64 L. Foglia, S. Vempati, B. T. Bonkano, L. Gierster, M. Wolf, S. Sadofev and J. Stähler, *Struct. Dyn.*, 2019, **6**, 034501.
65 M. A. Versteegh, T. Kuis, H. T. Stoof and J. I. Dijkhuis, *Phys. Rev. B: Condens. Matter Mater. Phys.*, 2011, **84**, 035207.
66 H. Zhu, N. Song, W. Rodríguez-Córdoba and T. Lian, *J. Am. Chem. Soc.*, 2012, **134**, 4250–4257.
67 G. Grimaldi, J. J. Geuchies, W. van der Stam, I. du Fossé, B. Brynjarsson, N. Kirkwood, S. Kinge, L. D. Siebbeles and A. J. Houtepen, *Nano Lett.*, 2019, **19**, 3002–3010.
68 D. P. Morgan and D. F. Kelley, *J. Phys. Chem. C*, 2020, **124**, 8448–8455.
69 T. Labrador and G. Dukovic, *J. Phys. Chem. C*, 2020, **124**, 8439–8447.
70 N. V. Tepliakov, M. Y. Leonov, A. V. Baranov, A. V. Fedorov, I. D. Rukhlenko, A. V. Fedorov, A. V. Baranov, I. D. Rukhlenko, T. S. Perova and K. Berwick, *Opt. Express*, 2016, **24**, A52–A57.
71 K. Tvrdy, P. A. Frantsuzov and P. V. Kamat, *Proc. Natl. Acad. Sci. U. S. A.*, 2011, **108**, 29–34.
72 G. Nagamine, T. A. C. Ferreira, D. B. Almeida, J. C. Lemus, J. H. Chang, B. G. Jeong, W. K. Bae and L. A. Padilha, *ACS Photonics*, 2022, **9**, 156–162.
73 D. R. Baker and P. V. Kamat, *Langmuir*, 2010, **26**, 11272–11276.
74 E. Cánovas, H. Wang, M. Karakus and M. Bonn, *Chem. Phys.*, 2016, **471**, 54–58.
75 C. Strothkämper, A. Bartelt, P. Sippel, T. Hannappel, R. Schütz and R. Eichberger, *J. Phys. Chem. C*, 2013, **117**, 17901–17908.
76 P. Kumar and S. K. Pal, *Phys. Chem. Chem. Phys.*, 2016, **18**, 29571–29581.
77 L. Gundlach, R. Ernstorfer and F. Willig, *Appl. Phys. A: Mater. Sci. Process.*, 2007, **88**, 481–495.
78 M. Borgwardt, M. Wilke, T. Kampen, S. Mähl, M. Xiao, L. Spiccia, K. M. Lange, I. Y. Kiyan and E. F. Aziz, *Sci. Rep.*, 2016, **6**, 1–7.
79 M. Greben, P. Khoroshyy, I. Sychugov and J. Valenta, *Appl. Spectrosc. Rev.*, 2019, **54**, 758–801.
80 A. Dominguez, M. Lorke, A. L. Schoenhalz, A. L. Rosa, T. Frauenheim, A. R. Rocha and G. M. Dalpian, *J. Appl. Phys.*, 2014, **115**, 203720.
81 A. W. Achtstein, S. Ayari, S. Helmrich, M. T. Quick, N. Owschimikow, S. Jaziri and U. Woggon, *Nanoscale*, 2020, **12**, 23521–23531.
82 E. M. Y. Lee and W. A. Tisdale, *J. Phys. Chem. C*, 2015, **119**, 9005–9015.
83 J. Aldana, Y. A. Wang and X. Peng, *J. Am. Chem. Soc.*, 2001, **123**, 8844–8850.
84 Y. Liang, J. E. Thorne and B. A. Parkinson, *Langmuir*, 2012, **28**, 11072–11077.
85 P. Tiwana, P. Docampo, M. B. Johnston, H. J. Snaith and L. M. Herz, *ACS Nano*, 2011, **5**, 5158–5166.
86 B. W. Mcneil and N. R. Thompson, *Nat. Photonics*, 2010, **4**, 814–821.
87 M. Quintana, T. Edvinsson, A. Hagfeldt and G. Boschloo, *J. Phys. Chem. C*, 2007, **111**, 1035–1041.
88 M. Eyer, J. Frisch, S. Sadofev, N. Koch, E. J. W. List-Kratochvil and S. Blumstengel, *J. Phys. Chem. C*, 2017, **121**, 21955–21961.